Modeling, Analysis, and Parameters Design of *LC*-Filter-Integrated Quasi-*Z*-Source Indirect Matrix Converter

Shuo Liu, Baoming Ge, *Member, IEEE*, Yushan Liu, *Member, IEEE*, Haitham Abu-Rub, *Senior Member, IEEE*, Robert S. Balog, *Senior Member, IEEE*, and Hexu Sun, *Senior Member, IEEE*

***Abstract*—Through coupling the impedance network between the grid and the conventional indirect matrix converter (IMC), the *LC*-filter-integrated quasi-Z-source (qZS) IMC overcomes the 0.866 voltage gain limitation of the conventional IMC and also avoids the input filter that is required to mitigate current harmonics of the conventional qZS matrix converters. This paper further investigates the voltage boosting and *LC* filtering function of the *LC*-filter-integrated qZS IMC. The voltage gain, the filtering function, and qZS network parameters design are presented using a small-signal model and circuit analysis. Simulation and experimental results validate the built model, the voltage gain analysis, and the parameters design of this type of qZS IMC. The input current of the *LC*-filter-integrated qZS network is compared to the conventional Z-source and qZS IMCs to investigate the integrated *LC* filtering capability. The experimental results verify that the *LC*-filter-integrated qZS network provides the necessary filtering function. Thus, the traditional input filter can be eliminated, which reduces the cost, power loss, volume, and weight for the overall system, when compared with the other conventional topologies that require the input filter, even those with impedance-source networks.**

***Index Terms*—Filter, matrix converter, modeling, quasi-Z-source inverter, voltage gain.**

I. Introduction

A matrix converter (MC) directly connects an ac source to an ac load without using intermediate energy storage. It has attracted the attention of academia and industry because it is an all-silicon power converter cell with the following features: 1) simple and compact power circuit without dc-link capacitor; 2) output voltage with variable amplitude and variable frequency; 3) sinusoidal input/output currents; and 4) unity power factor operation at input side [1]–[3]. There are two types of MC topologies: direct MC (DMC) and indirect MC (IMC), shown in Fig. 1(a) and (b), respectively [3], [4]. The DMC and IMC have similar system-level performance, including current harmonics, maximum voltage gain of 0.866, and in practice both like other converters, requiring input filters as shown in Fig. 1. IMC does not have the current commutation problem of the DMC, making it more attractive in applications, and is thus the focus of the topology in this paper.

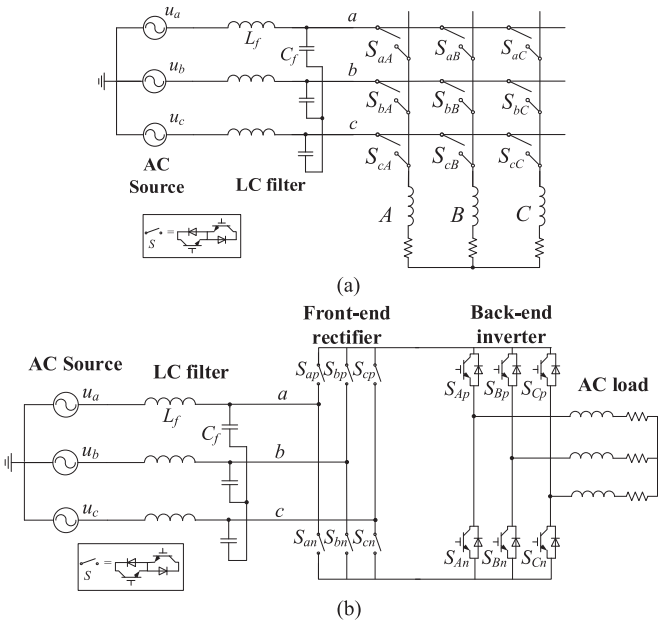

Fig. 1. Topologies of conventional (a) DMC, and (b) IMC.

To overcome the voltage gain limitation of the MC, overmodulation strategies have been proposed to increase the output voltage [5], [6], but have the side-effect of creating low-order harmonics at both the output voltage and the input current. Another approach is to use a step-up transformer connected between the power supply and the MC. It is a simple way to raise the output voltage, but at the expense of volume, weight, cost, and efficiency [7]. In yet another approach, an ac chopper was combined with the MC, creating the so-called matrix-reactance frequency converter (MRFC), which enables a voltage gain greater than unity [8]. However, it increased the control complexity and added extra power conversion stage, while the

Manuscript received October 18, 2015; revised January 11, 2016; accepted March 19, 2016. Date of publication April 13, 2016; date of current version June 24, 2016. This work was made possible by NPRP-EP Grant # X-033-2-007 from the Qatar National Research Fund (a member of Qatar Foundation) (Sections I, II, IV, and VI), the National Natural Science Foundation of China (Grant 51477008) (Sections III and V), and Beijing Natural Science Foundation (Grant 3152021) (Section VII). The statements made herein are solely the responsibility of the authors. Recommended for publication by Associate Editor C. Xia.

S. Liu is with the Department of Electrical Engineering, North China University of Technology, Beijing, 100144, China (e-mail: 1339721457@qq.com).

B. Ge is with the Department of Electrical and Computer Engineering, Texas A&M University, College Station, TX 77843 USA (e-mail: baomge@gmail.com).

Y. Liu and H. Abu-Rub are with the Department of Electrical and Computer Engineering, Texas A&M University at Qatar, Qatar Foundation, Doha 23874, Qatar (e-mail: yushan.liu@qatar.tamu.edu; haitham.abu-rub@qatar.tamu.edu).

R. S. Balog is with the Department of Electrical and Computer Engineering, Texas A&M University at Qatar, Qatar Foundation, Doha 23874, Qatar, and also with the Department of Electrical and Computer Engineering, Texas A&M University, College Station, TX 77843 USA (e-mail: Robert.Balog@ieee.org).

H. Sun is with the School of Control Science and Engineering, Hebei University of Technology, Tianjin, 300130, China (e-mail: hxsun@hebut.edu.cn).

Color versions of one or more of the figures in this paper are available online at http://ieeexplore.ieee.org

Digital Object Identifier 10.1109/TPEL.2016.2553582

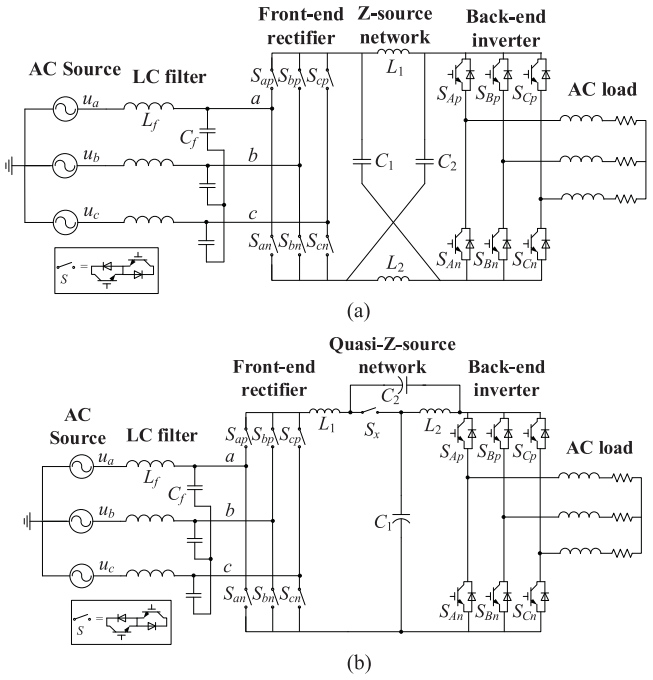

Fig. 2. ZS/qZS IMC with impedance-source network in dc link. (a) ZS IMC and (b) qZS IMC.

voltage transfer ratio highly relied on the circuit and load parameters [7].

The Z-source (ZS) and quasi-Z-source (qZS) inverters were developed to overcome the voltage limitation of buck-derived voltage-source inverters (VSIs). Further advantages include single-stage power conversion, short-circuit immunity, and wide input voltage capability [9]–[11]. These advantages retain when the ZS/qZS networks are embedded into the intermediate dc link of the IMC [12]–[14] and the sparse MC with reduced switches at rectifier side [15], [16]. Fig. 2(a) and (b) shows the ZS and qZS IMC, respectively, with impedance network in the dc link to overcome the voltage gain limit of the MC. They are lighter in weight, more compact in volume, and have less power loss than an IMC with a step-up transformer, even though bidirectional switches exist in the impedance network. Simple modification of the modulation enables the ZS/qZS IMC to operate without affecting the output of the MC. Thus, it provides voltage gain that is independent of the load without requiring a second power conversion stage, unlike the MRFC. However, embedding the qZS at the intermediate dc link means that the IMC is no longer an all-silicon MC cell.

Consider the ZS/qZS networks located at the ac input side. The ZS DMC [17], qZS IMC [18], and ZS IMC [19] were proposed to extend the voltage gain, as shown in Fig. 3(a), (b), and (c), respectively, while maintaining an all-silicon MC cell. The disadvantage is that the input currents are discontinuous which leads to higher total harmonic distortion (THD). Thus, an input filter, like the second-order *LC* filter shown in Fig. 3, is still required on the grid side to mitigate harmonic pollution and improve grid-tie power quality.

An *LC*-filter-integrated qZS IMC, shown in Fig. 4, was proposed in [19] to avoid the input filter of the conventional ZS/qZS IMC in Fig. 3. The qZS network links the ac source directly to the IMC. This novel qZS IMC has two important advantages:

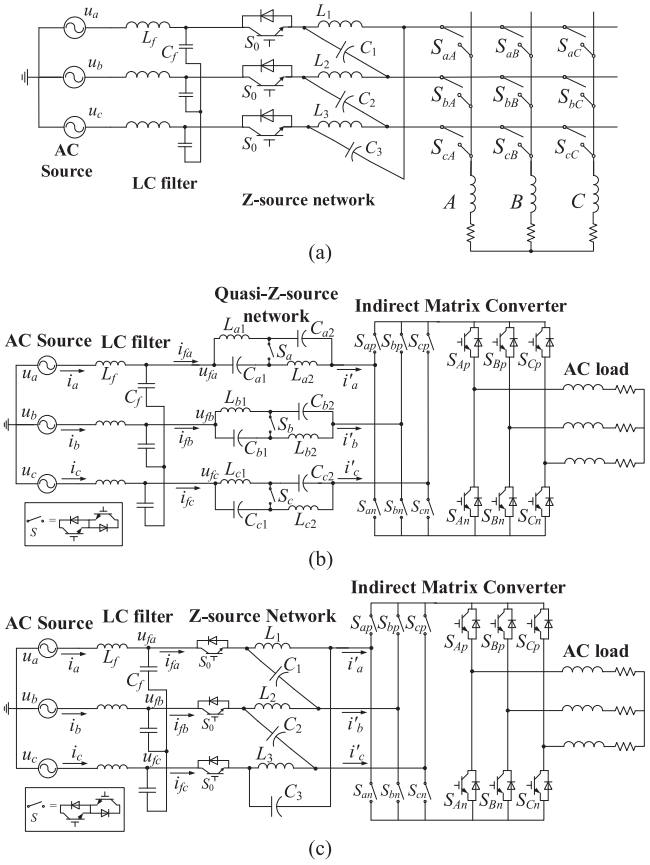

Fig. 3. ZS/qZS MCs with impedance-source network at ac input side. (a) ZS DMC [17], (b) qZS IMC [18], and (c) ZS IMC [19].

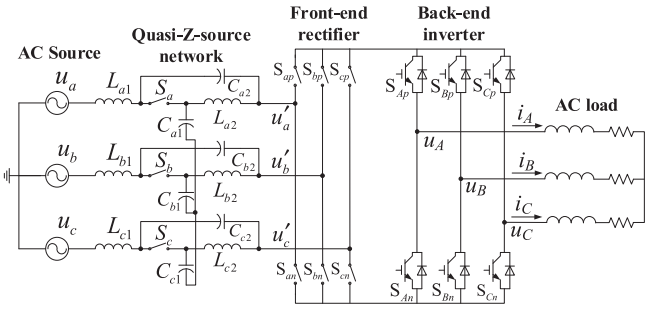

Fig. 4. *LC*-filter-integrated qZS IMC in [19].

1) voltage boost ability that overcomes the voltage gain limit of conventional MCs; and 2) second-order filtering function that avoids extra *LC* filter. In addition, it contains an all-silicon MC cell and retains all other advantages of the conventional MC and qZS inverters. Most importantly, the grid current is continuous and sinusoidal without requiring an extra *LC* filter. The benefits include reduced cost, low volume, low power loss, and low weight. The voltage gain, voltage and current ripple, passive components stress, power devices stress, etc., of the novel qZS IMC, the traditional qZS IMC in Fig. 3(b), and the ZS IMC in Fig. 3(c) were compared in [19]. The previous analysis and the comparison result in [19] show that the novel qZS IMC has more attractive applications in ac motor drives, than the traditional ZS/qZS MCs.

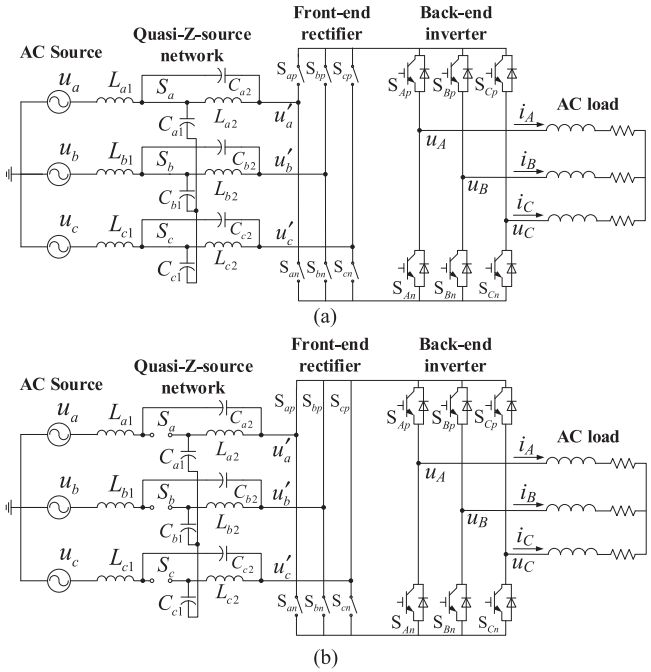

Fig. 5. Working states of the *LC*-filter-integrated qZS IMC. (a) Non-shoot-through state and (b) shoot-through state.

This paper further contributes to the model for the *LC*-filter-integrated qZS IMC by conducting an in-depth theoretical analysis of the voltage boosting and *LC* filtering functions, as well as an investigation of the impedance design method. Simulation and experimental results are presented to verify the model, the theoretical analysis, and the parameters design.

II. Operation Analysis of Novel qZS IMC

A. Discussed Topology

As shown in Fig. 4, the *LC*-filter-integrated qZS IMC is comprised of three parts: the qZS network, the front-end rectifier, and the back-end inverter. The qZS network includes three coupled inductors (L_{a1} coupled to L_{a2}, L_{b1} coupled to L_{b2}, L_{c1} coupled to L_{c2}), six capacitors C_{a1}, C_{a2}, C_{b1}, C_{b2}, C_{c1}, and C_{c2}, three bidirectional switches S_a, S_b, and S_c, where the three switches can operate from one gate signal S_x. This topology has two modes of operation, buck and boost modes, realized by two states, shoot-through and non-shoot-through states.

B. Buck Operation

In the buck operating mode, the three switches S_a, S_b, and S_c are turned ON. The front-end rectifier and the back-end inverter are modulated to achieve the desired output voltage in the same way as a conventional IMC.

C. Boost Operation

The boost mode operation includes two states, i.e., shoot-through state and non-shoot-through state, as shown in Fig. 5. The voltage boost is achieved by adjusting the shoot-through time.

1) Non-Shoot-Through State: In the non-shoot-through state of Fig. 5(a), the three switches S_a, S_b, and S_c are turned ON and the front-end rectifier works in the conventional way. During this period, the inductors discharge to the capacitors; each output phase voltage of the qZS network is the sum of two capacitor voltages. Due to $L_{a1}=L_{a2}=L_{b1}=L_{b2}=L_{c1}=L_{c2}=L$ and $C_{a1}=C_{a2}=C_{b1}=C_{b2}=C_{c1}=C_{c2}=C$, from Fig. 5(a), the following expressions can be obtained:

$$Lp\mathbf{I}_{L1} = \mathbf{u}_i - \mathbf{u}_{C1} - R_L\mathbf{I}_{L1} \tag{1}$$

$$Lp\mathbf{I}_{L2} = -\mathbf{u}_{C2} - R_L\mathbf{I}_{L2} \tag{2}$$

$$Lp\mathbf{I}_{L1} = \mathbf{u}_i + \mathbf{u}_{C2} - \mathbf{u}' - R_L\mathbf{I}_{L1} \tag{3}$$

$$Cp\mathbf{u}_{C1} = \mathbf{I}_{L1} - \mathbf{I}' \tag{4}$$

$$Cp\mathbf{u}_{C2} = \mathbf{I}_{L2} - \mathbf{I}' \tag{5}$$

where $p=d/dt$; the qZS inductor-L_1 current $\mathbf{I}_{L1}=[\,i_{La1}\;\; i_{Lb1}\;\; i_{Lc1}\,]^T$, i.e., the grid current; the qZS inductor-L_2 current $\mathbf{I}_{L2}=[\,i_{La1}\;\; i_{Lb1}\;\; i_{Lc1}\,]^T$; the qZS capacitor-$C_1$ voltage $\mathbf{u}_{C1}=[\,u_{Ca1}\;\; u_{Cb1}\;\; u_{Cc1}\,]^T$; the qZS capacitor-$C_2$ voltage $\mathbf{u}_{C2}=[\,u_{Ca1}\;\; u_{Cb1}\;\; u_{Cc1}\,]^T$; the grid voltage $\mathbf{u}_i=[\,u_a\;\; u_b\;\; u_c\,]^T$; the qZS network output voltage $\mathbf{u}'=[\,u'_a\;\; u'_b\;\; u'_c\,]^T$; the qZS network output current $\mathbf{I}'=[i'_a\;\; i'_b\;\; i'_c]^T$; R_L is the stray resistance of inductors.

2) Shoot-Through State: During the shoot-through state, the three switches S_a, S_b, and S_c are turned OFF at the same time, the input side of front-end rectifier is short circuit, and hence both the qZS inductors in each phase charge. Fig. 5(b) shows the equivalent circuit, where the switches of qZS network are OFF and the upper switches of front-end rectifier are ON. From Fig. 5(b), there are

$$Lp\mathbf{I}_{L1} = \mathbf{u}_i + \mathbf{u}_{C2} - R_L\mathbf{I}_{L1} \tag{6}$$

$$Lp\mathbf{I}_{L2} = \mathbf{u}_{C1} - R_L\mathbf{I}_{L2} \tag{7}$$

$$Cp\mathbf{u}_{C2} = -\mathbf{I}_{L1},\; Cp\mathbf{u}_{C1} = -\mathbf{I}_{L2}. \tag{8}$$

If the shoot-through time is T_0 in one switching cycle T_s, shoot-through duty cycle is defined as $D=T_0/T_s$. The output voltage $\mathbf{u}'$ of qZS network can be boosted to the desired value through changing shoot-through duty cycle *D*.

III. Small-Signal Modeling of qZS IMC

The state-space model is obtained from (1)–(8)

$$\begin{cases} Lp\mathbf{I}_{L1} = (1-D)(\mathbf{u}_i + \mathbf{u}_{C2} - \mathbf{u}' - R_L\mathbf{I}_{L1}) \\ \qquad\qquad + D(\mathbf{u}_i + \mathbf{u}_{C2} - R_L\mathbf{I}_{L1}) \\ Lp\mathbf{I}_{L2} = (1-D)(-\mathbf{u}_{C2} - R_L\mathbf{I}_{L2}) + D(\mathbf{u}_{C1} - R_L\mathbf{I}_{L2}) \\ Cp\mathbf{u}_{C1} = (1-D)(\mathbf{I}_{L1} - \mathbf{I}') - D\mathbf{I}_{L2} \\ Cp\mathbf{u}_{C2} = (1-D)(\mathbf{I}_{L2} - \mathbf{I}') - D\mathbf{I}_{L1}. \end{cases} \tag{9}$$

Note that in (9) and the rest of this paper, the vectors $\mathbf{I}_{L1}$, $\mathbf{I}_{L2}$, $\mathbf{u}_{C1}$, $\mathbf{u}_{C2}$, $\mathbf{u}'$, and $\mathbf{u}_i$ are replaced by i_{L1}, i_{L2}, u_{C1}, u_{C2}, u', and u_i; the equations of each phase rather than three phases can be obtained, as shown in (10) that is the average state-space

equations of one phase. Consider the symmetric case in which $L_{a1}=L_{a2}=L_{b1}=L_{b2}=L_{c1}=L_{c2}=L$ and $C_{a1}=C_{a2}=C_{b1}=C_{b2}=C_{c1}=C_{c2}=C$, so $i_{L1}=i_{L2}=i_L$. Thus, (10) follows:

$$\begin{bmatrix} L & 0 & 0 \\ 0 & C & 0 \\ 0 & 0 & C \end{bmatrix} p \begin{bmatrix} i_L \\ u_{C1} \\ u_{C2} \end{bmatrix} = \begin{bmatrix} -R_L & D-1 & D \\ 1-2D & 0 & 0 \\ 1-2D & 0 & 0 \end{bmatrix} \times \begin{bmatrix} i_L \\ u_{C1} \\ u_{C2} \end{bmatrix} + \begin{bmatrix} 1 & 0 \\ 0 & D-1 \\ 0 & D-1 \end{bmatrix} \begin{bmatrix} u_i \\ i' \end{bmatrix}. \tag{10}$$

Small-signal perturbations are included in the input voltage, output current of qZS network, and the shoot-through duty cycle, respectively, which results in $u_i=\bar{u}_i+\hat{u}_i$, $i'=\bar{i}'+\hat{i}'$, and $d=D+\hat{d}$. From (10), the small-signal state equations are

$$\begin{bmatrix} L p\hat{i}_L \\ C p\hat{u}_{C1} \\ C p\hat{u}_{C2} \end{bmatrix} = \begin{bmatrix} -R_L & D-1 & D \\ 1-2D & 0 & 0 \\ 1-2D & 0 & 0 \end{bmatrix} \begin{bmatrix} \hat{i}_L \\ \hat{u}_{C1} \\ \hat{u}_{C2} \end{bmatrix} + \begin{bmatrix} 1 & 0 & \bar{u}_{C1}+\bar{u}_{C2} \\ 0 & D-1 & \bar{i}'-2\bar{i}_L \\ 0 & D-1 & \bar{i}'-2\bar{i}_L \end{bmatrix} \begin{bmatrix} \hat{u}_i \\ \hat{i}' \\ d \end{bmatrix}. \tag{11}$$

In the s-domain, the small-signal expressions for the capacitor voltages and inductor currents are

$$\begin{cases} \hat{u}_{C1}(s) = G_{C1\mathrm{ui}}(s)\,\hat{u}_i(s) + G_{C1\mathrm{ii}}(s)\,\hat{i}'(s) + G_{C1d}(s)\,\hat{d}(s) \\ \hat{u}_{C2}(s) = G_{C2\mathrm{ui}}(s)\,\hat{u}_i(s) + G_{C2\mathrm{ii}}(s)\,\hat{i}'(s) + G_{C2d}(s)\,\hat{d}(s) \\ \hat{i}_L(s) = G_{L\mathrm{ui}}(s)\,\hat{u}_i(s) + G_{L\mathrm{ii}}(s)\,\hat{i}'(s) + G_{Ld}(s)\,\hat{d}(s) \end{cases} \tag{12}$$

where the G terms are in (13)–(21) shown at the bottom of the page.

IV. Voltage Gain Investigation

A. Modeling IMC

The input-current space vector modulation (SVM) and output-voltage SVM are applied to the front-end rectifier and the back-end inverter, respectively, of the *LC*-filter-integrated qZS IMC [19].

For the front-end rectifier, the switching modes of the rectifier stage can be classified as active vector state and zero vector state, and the shoot-through zero vector is inserted during the rectifier's zero vector states. In the shoot-through zero vector, the three-phase source is short-circuited to boost voltage. The vector duty cycles are calculated from

$$\begin{cases} d_\alpha = m_i \sin\left(\frac{\pi}{3}-\theta_i\right) \\ d_\beta = m_i \sin\theta_i \\ d_s = \mathrm{const}\,(d_s < 1-d_\alpha-d_\beta) \\ d_{or} = 1-d_\alpha-d_\beta-d_s \end{cases} \tag{22}$$

$$G_{C1\mathrm{ui}}(s) = \frac{C(1-2D)}{s^2C^2L+sR_LC^2+(1-D)(1-2D)C-DC(1-2D)} \tag{13}$$

$$G_{C1\mathrm{ii}}(s) = \frac{(D-1)C(sL+R_L)}{s^2C^2L+sR_LC^2+(1-D)(1-2D)C-DC(1-2D)} \tag{14}$$

$$G_{C1d}(s) = \frac{(1-2D)C(\bar{u}_{C1}+\bar{u}_{C2})+C(sL+R_L)(\bar{i}'-2\bar{i}_L)}{s^2C^2L+sR_LC^2+(1-D)(1-2D)C-DC(1-2D)} \tag{15}$$

$$G_{C2\mathrm{ui}}(s) = \frac{C(1-2D)}{s^2C^2L+sR_LC^2+(1-D)(1-2D)C-DC(1-2D)} \tag{16}$$

$$G_{C2\mathrm{ii}}(s) = \frac{(D-1)C(sL+R_L)}{s^2C^2L+sR_LC^2+(1-D)(1-2D)C-DC(1-2D)} \tag{17}$$

$$G_{C2d}(s) = \frac{(1-2D)C(\bar{u}_{C1}+\bar{u}_{C2})+C(sL+R_L)(\bar{i}'-2\bar{i}_L)}{s^2C^2L+sR_LC^2+(1-D)(1-2D)C-DC(1-2D)} \tag{18}$$

$$G_{L\mathrm{ui}}(s) = \frac{C^2s}{s^2C^2L+sR_LC^2+(1-D)(1-2D)C-DC(1-2D)} \tag{19}$$

$$G_{L\mathrm{ii}}(s) = \frac{(D-1)^2C+D(D-1)C}{s^2C^2L+sR_LC^2+(1-D)(1-2D)C-DC(1-2D)} \tag{20}$$

$$G_{Ld}(s) = \frac{sC^2(\bar{u}_{C1}+\bar{u}_{C2})+(D-1)C(\bar{i}'-2\bar{i}_L)+DC(\bar{i}'-2\bar{i}_L)}{s^2C^2L+sR_LC^2+(1-D)(1-2D)C-DC(1-2D)} \tag{21}$$

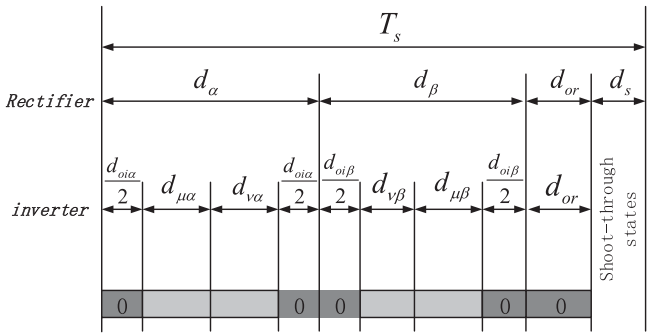

Fig. 6. Switching sequence for the *LC*-filter-integrated qZS IMC.

where m_i is the modulation index of the front-end rectifier; θ_i is the input current vector angle; d_α, d_β, d_s, and d_{or} are the duty cycles of different current vectors in one switching period.

The back-end inverter operates the same as a conventional VSI, which has six active vectors and two zero vectors; the duty cycles are calculated by

$$\begin{cases} d_\mu = m_o \sin\left(\dfrac{\pi}{3} - \theta_o\right) \\ d_\nu = m_o \sin\theta_o \\ d_{oi} = 1 - d_\mu - d_\nu \end{cases} \tag{23}$$

where m_o is the modulation index of the back-end inverter; θ_o is the output voltage vector angle; d_μ, d_ν, and d_{oi} are the duty cycles of output voltage active vectors and zero vector, respectively.

To balance the input currents and the output voltages in the switching period, the modulation pattern should produce all combinations of the rectification and inversion switching states; the final switching sequence is shown in Fig. 6. The corresponding duty cycles can be calculated by

$$\begin{cases} d_{\mu\alpha} = d_\mu \cdot d_\alpha \\ d_{\mu\beta} = d_\mu \cdot d_\beta \\ d_{\nu\alpha} = d_\nu \cdot d_\alpha \\ d_{\nu\beta} = d_\nu \cdot d_\beta \\ d_{oi\alpha} = d_{oi} \cdot d_\alpha \\ d_{oi\beta} = d_{oi} \cdot d_\beta \end{cases} \tag{24}$$

where T_s is the switching period; $d_{\mu\alpha}$, $d_{\mu\beta}$, $d_{\nu\alpha}$, $d_{\nu\beta}$, $d_{oi\alpha}$, and $d_{oi\beta}$ are the duty cycles of different output voltage vectors in one switching period.

The obtained switching signals are utilized to operate the qZS IMC's power switches, where the rectifier side has six bidirectional switches and the inverter side has six insulated-gate bipolar transistors, both connected by a fictitious dc link (without capacitor or dc/dc converter). The switching function of a single switch for both bridges is defined as

$$S_{xy} = \begin{cases} 1, & \text{Switch } S_{xy} \quad \text{closed} \\ 0, & \text{Switch } S_{xy} \quad \text{open} \end{cases}, \; x = a, b, c, A, B, C; y = p, n. \tag{25}$$

For the rectifier side, the dc-link voltage u_{dc} is a function of the rectifier switches' switching states and the output voltages $\mathbf{u}'$ of qZS network, as follows:

$$u_{dc} = \begin{bmatrix} S_{ap} - S_{an} & S_{bp} - S_{bn} & S_{cp} - S_{cn} \end{bmatrix} \cdot \mathbf{u}'. \tag{26}$$

The output currents $\mathbf{I}'$ of qZS network are functions of the rectifier switches' switching states and the dc-link current i_{dc} as follows:

$$\mathbf{I}' = \begin{bmatrix} S_{ap} - S_{an} \\ S_{bp} - S_{bn} \\ S_{cp} - S_{cn} \end{bmatrix} \cdot i_{dc}. \tag{27}$$

For the inverter side, the dc-link current i_{dc} is a function of the inverter switches' switching states and the output currents i_A, i_B, and i_C as

$$i_{dc} = \begin{bmatrix} S_{Ap} & S_{Bp} & S_{Cp} \end{bmatrix} \cdot \begin{bmatrix} i_A \\ i_B \\ i_C \end{bmatrix} = \begin{bmatrix} S_{Ap} & S_{Bp} & S_{Cp} \end{bmatrix} \cdot \mathbf{I}_o. \tag{28}$$

Finally, the output voltages of inverter stage are synthesized as a function of the inverter switches' switching states and the dc-link voltage u_{dc} as

$$\mathbf{u}_o = \begin{bmatrix} u_A \\ u_B \\ u_C \end{bmatrix} = \begin{bmatrix} S_{Ap} - S_{An} \\ S_{Bp} - S_{Bn} \\ S_{Cp} - S_{Cn} \end{bmatrix} \cdot u_{dc}. \tag{29}$$

Equations (25)–(29) present the mathematical model of the IMC on the basis of the switching states in the rectifier and inverter stages, respectively. The operational condition of the IMC is that the dc-link voltage must be always positive or zero, i.e., $u_{dc} \geq 0$.

B. Voltage Gain Analysis

In steady state, the inductor average voltage and the capacitor average current are zero over one switching period. From (9), there are

$$\begin{cases} u_{C1} = \dfrac{(1-D)\,u_i - R_L i_L}{1-2D} \\ u_{C2} = \dfrac{D u_i - R_L i_L}{1-2D} \\ u' = \dfrac{u_i - 2R_L i_L}{1-2D} \\ i_{L1} = i_{L2} = i_L \\ i' = \dfrac{1-2D}{1-D} i_L. \end{cases} \tag{30}$$

From (30), if the resistance of inductor is ignored, the voltage boost factor *B* is expressed as

$$B = \frac{u'}{u_i} = \frac{1}{1-2D}. \tag{31}$$

From (22)–(29), the average dc-link current I_{dc} and the virtual dc-link peak voltage V_{dc} of the IMC are obtained as

$$I_{dc} = \frac{1}{1-D} I_{om}\, m_o \cos\theta_{\text{out}}, \; V_{dc} = \frac{3}{2} V_{im}\, m_i \cos\theta_{\text{ind}} \tag{32}$$

where I_{om} denotes the amplitude of inverter output current $\mathbf{I}_o$, θ_{out} denotes the output displacement angle, V_{im} denotes the amplitude of rectifier input voltage $\mathbf{u}'$, and θ_{ind} denotes the input displacement angle.

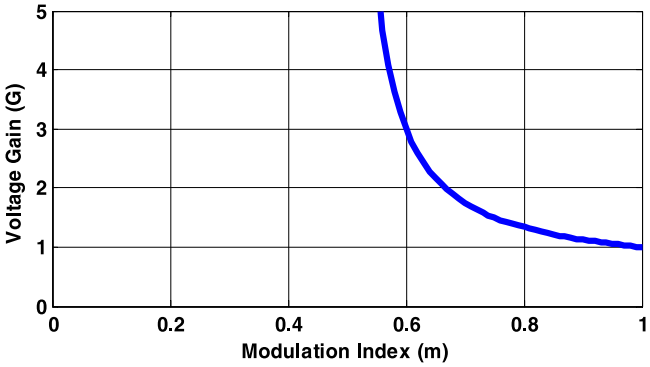

Fig. 7. Voltage gain versus modulation index of the novel qZS IMC.

Applying power balance at the inverter side results in the expression

$$(1-D)V_{dc}I_{dc} = \frac{3}{2}V_{om}I_{om}\cos\theta_{\text{out}} \tag{33}$$

where V_{om} denotes the amplitude of inverter output voltage $\mathbf{u}_o$.

The input current vector $\mathbf{I}_{L1}$ collinear with the input voltage vector $\mathbf{u}_i$ in Fig. 4 to achieve unity power factor [20]. From (32) and (33), the inverter output voltage amplitude is associated with the input voltage amplitude of

$$V_{om} = V_{im}m_i m_o. \tag{34}$$

Then, from (31) and (34), the voltage gain *G* of the discussed qZS IMC is obtained as

$$G = \frac{V_{om}}{U_m} = \frac{m_i m_o}{1-2D} = Bm \tag{35}$$

where U_m denotes the amplitude of grid voltage, and $m = m_i m_o$ denotes the modulation index.

Fig. 7 shows the voltage gain versus the modulation index *m*. The *LC*-filter-integrated qZS IMC can achieve the voltage gain greater than 0.866 by choosing the modulation index (*m*) and shoot-through duty ratio (*D*).

V. qZS Network's Filtering Function Investigation

The filtering function of the qZS network is investigated through the circuit large signal analysis and *s*-domain small-signal analysis.

A. Circuit Large Signal Analysis

As shown in Fig. 4, the grid current $\mathbf{I}_{L1}$ is continuous due to the qZS inductor L_{a1}, L_{b1}, and L_{c1}; thus, the novel qZS IMC does not require additional input filter but has the advantages of voltage boost function and conventional IMC. The main difference between the conventional ZS/qZS MCs in Fig. 3 and the *LC*-filter-integrated qZS IMC in Fig. 4 is that the latter has no explicit input filter yet draws continuous ac current from the grid, which demonstrates that the *LC*-filter-integrated qZS network has the filtering function. On the other hand, the converters in Fig. 3 require additional *LC* filters to draw a continuous current from the grid; otherwise, discontinuous ac current will flow through the grid. In addition, the discontinuous input currents of ZS and qZS networks in Fig. 3 have much higher current peak values than those in Fig. 4, which causes high current stress to power devices.

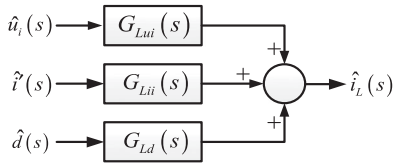

Fig. 8. Signal flow diagram of small-signal model of the grid currents $\mathbf{I}_{L1}$.

For the conventional ZS/qZS MCs, as shown in Fig. 3, the additional *LC* filter is required to filter the high-frequency components from the input currents of ZS/qZS network. For example, the input currents i_{fa}, i_{fb}, and i_{fc} of qZS network in Fig. 3(b) are discontinuous and have high-frequency components, which are not allowed to flow into the grid due to high harmonic components. Therefore, the additional *LC* filter is used between the grid and qZS network in Fig. 3(b), which results in grid currents i_a, i_b, and i_c in Fig. 3(b) that are continuous and have low harmonic components. The employed *LC* filter is a second-order system; considering phase *a* in Fig. 3(b), the filter is modeled as

$$\begin{cases} L_f p i_a = (u_a - u_{fa}) - R_f i_a \\ C_f p u_{fa} = i_a - i_{fa} \end{cases}$$
$$\Rightarrow \left(L_f C_f p^2 + R_f C_f p + 1\right) i_a = i_{fa} + C_f p u_a \tag{36}$$

where L_f is the filter inductance; C_f is the filter capacitance; R_f is the filter damping resistance; u_{fa} and i_{fa} are the phase-*a* input voltage and current of qZS network, respectively; u_a and i_a are the grid voltage and current in the phase *a*, respectively, as shown in Fig. 3(b).

For the *LC*-filter-integrated qZS IMC, the following expression follows from the large signal state-space equations given in (9):

$$\begin{cases} Lp(i_{L1}+i_{L2}) = u_i - (1-2D)u' - R_L(i_{L1}+i_{L2}) \\ Cp(u_{C1}+u_{C2}) = (1-2D)(i_{L1}+i_{L2}) - 2(1-D)i'. \end{cases} \tag{37}$$

From (30), the output voltage of qZS network in Fig. 4 is $u' = u_{C1} + u_{C2}$. Then, from (37), the second-order system of qZS network in Fig. 4 is obtained as

$$\left[LCp^2 + R_L Cp + (1-2D)^2\right](i_{L1}+i_{L2})$$
$$= 2(1-D)(1-2D)\ i' + Cpu_i.$$

Due to $i_{L1} = i_{L2}$, there is

$$\left[LCp^2 + R_L Cp + (1-2D)^2\right] i_{L1}$$
$$= (1-D)(1-2D)\ i' + 0.5\,Cpu_i. \tag{38}$$

It shows that the (38) has the same expression with (36), but they have the different coefficients, which demonstrates that the qZS network between the grid and the IMC bridges has filtering capability in Fig. 4.

B. s-Domain Small-Signal Analysis

The grid currents $\mathbf{I}_{L1}$ in Fig. 4 are given in (12) as the small-signal model. When the signal flow diagram is employed, it is shown in Fig. 8.

$G_{L\mathrm{ui}}(s)$ is the transfer function related to the grid voltage $\mathbf{u}_i$, which is independent of the output current $\mathbf{I}'$ of qZS network; $G_{L\mathrm{ii}}(s)$ is the transfer function related to the output current $\mathbf{I}'$ of qZS network, which is independent of the grid voltage $\mathbf{u}_i$; $G_{Ld}(s)$ is the transfer function related to the shoot-through duty ratio D. $G_{L\mathrm{ii}}(s)$ presents the relation between the current $\mathbf{I}'$ and grid currents $\mathbf{I}_{L1}$, which has the expression in (20) and is the same to a conventional LC filter, so the qZS network of novel qZS IMC has filtering capability with $G_{L\mathrm{ii}}(s)$.

From (20), the characteristic frequency ω_n and damping factor ζ of $G_{L\mathrm{ii}}(s)$ are

$$\begin{cases} \omega_n = \dfrac{1-2D}{\sqrt{LC}} \\ \zeta = \dfrac{(R_L+R_C)C}{2(1-2D)\sqrt{LC}} \end{cases} \tag{39}$$

which shows that the filtering performance of $G_{L\mathrm{ii}}(s)$ is related to the capacitance and inductance of qZS network, and the shoot-through duty cycle.

Fig. 9 shows the Bode plots of qZS network transfer function $G_{L\mathrm{ii}}(s)$. It can be seen that with the increase of qZS inductance, qZS capacitance, and shoot-through duty ratio, the resonant frequency and crossover frequency of $G_{L\mathrm{ii}}(s)$ decrease, benefiting to the increase of system stability. In addition, when the qZS inductance and qZS capacitance increase, the amplitude-frequency characteristic changes steeply and the quality factor increases, whereas the amplitude-frequency characteristic changes gently and the quality factor decreases when the shoot-through duty ratio increases.

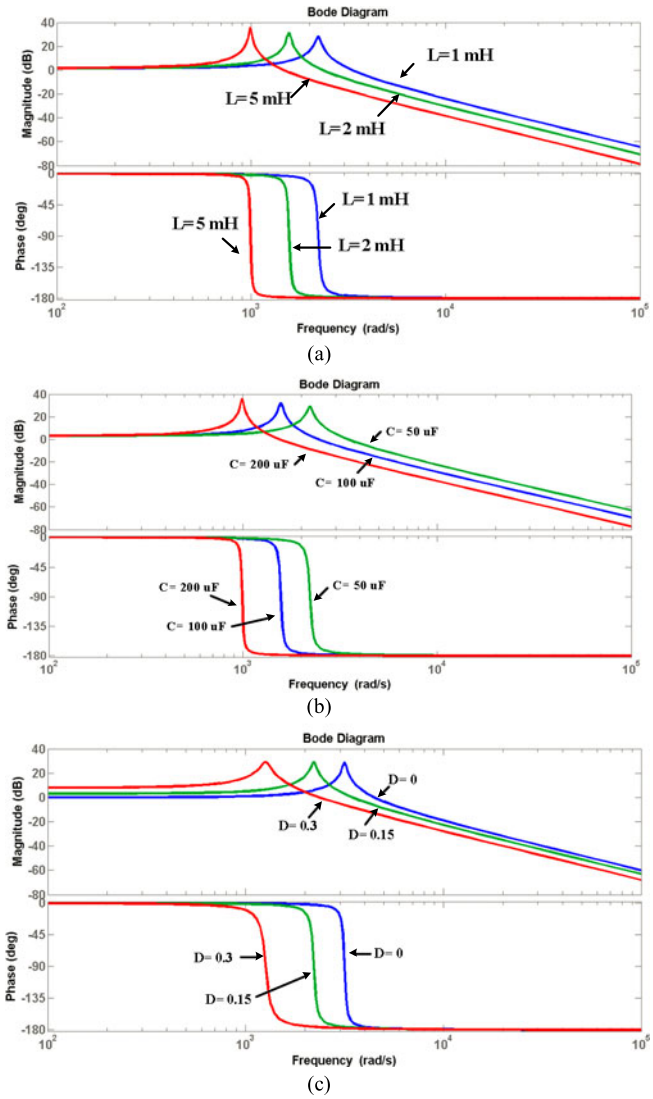

Fig. 9. Bode diagrams of qZS network transfer function $G_{L\mathrm{ii}}(s)$. (a) At inductance changes, (b) at capacitance changes, and (c) at changes of shoot-through duty cycle.

VI. Parameters Design of qZS Network

From the analysis of aforementioned filtering function, the qZS inductor must limit the switching frequency ripple current to within the required limit. For instance, the grid current THD should be less than 5% of the fundamental current required by the IEEE 519 [21]. The qZS capacitor should limit switching frequency ripple of the output voltage $\mathbf{u}'$ of qZS network. In addition, it is necessary that the grid current is drawn at the unity power factor, i.e., the input displacement angle is close to zero at the fundamental frequency f_0 of the grid.

A. Switching Frequency Ripple Limit

From Fig. 5(a), when using the phase a as example, we can calculate the inductor current ripple as

$$\Delta i_L = \frac{|u_a - u_{Ca1}|\,(1-D)}{f_s L}. \tag{40}$$

From Fig. 5(b), the capacitor voltage ripple is calculated as

$$\Delta u_C = \frac{i_{La1} D T_s}{C}. \tag{41}$$

Assume that the desired inductor current ripple is within $k_1 I_{\mathrm{rated}}$, and the desired capacitor voltage ripple is within $k_2 V_{C,\mathrm{rated}}$, where k_1 and k_2 are coefficients; and I_{rated} and $V_{C,\mathrm{rated}}$ are the rated grid current and the capacitor-C_2 rated voltage, respectively, where $V_{C,\mathrm{rated}} = DV_s/(1–2D)$ with V_s for the rms grid voltage. It can be seen that k_1 and k_2 are related to the switching frequency ripple of grid current $\mathbf{I}_{L1}$ and the output voltage $\mathbf{u}'$ of the qZS network. Then, the qZS inductance is constrained by

$$L \geq \frac{U_m D\,(1-D)}{(1-2D)\,f_s k_1 I_{\mathrm{rated}}}. \tag{42}$$

The qZS capacitance is constrained by

$$C \geq \frac{I_{\mathrm{rated}}\,(1-2D)}{f_s k_2 V_s}. \tag{43}$$

The selection of k_1 and k_2 should consider the following factors: 1) a large k_1 is preferable to have a smaller inductance, but which causes higher harmonic components injected into the grid; therefore, the k_1 should be less than 5%; 2) a large k_2 is preferable to have a smaller capacitance, but which may affect the output voltage quality of qZS IMC. The virtual dc-link voltage u_{dc} of qZS IMC is the line-to-line voltage of qZS

TABLE I
PARAMETERS IN SIMULATION AND EXPERIMENT

Description	Value
Power rating	1.5 kW
Capacitance of ZS/qZS network	300 μF
Inductance of ZS/qZS network	2 mH
Shoot-through duty cycle	0.15
Switching frequency, f_s	10 kHz
Input voltage frequency, f_0	50 Hz
Load resistance, R_L	5 Ω
Load inductance, L_L	3 mH

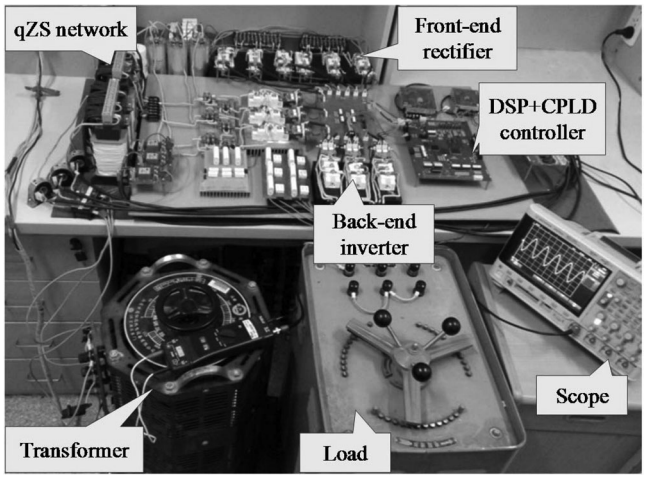

Fig. 10. Experimental setup of the ZS/qZS IMC.

network output; from (31), the maximum value of u_{dc} is

$$u_{dc,\max} = \sqrt{3}u'_{a,\max} = \frac{\sqrt{3}}{1-2D}u_{a,\max} = \frac{\sqrt{3}}{D}u_{Ca2,\max}. \tag{44}$$

When $D = 1/3$, $u_{dc,\max} = 5.19 \times u_{Ca2,\max}$, so $k_2 V_{C,\text{rated}} = u_{dc,\max} \times k_2/5.19$. Due to the doubled high-frequency voltage ripple on the output voltage of qZS network, which is from the two series capacitors C_1 and C_2 of qZS network at the non-shoot-through state, the high-frequency voltage ripple ratio of the virtual dc-link voltage is

$$\delta = 2k_2 V_{C,\text{rated}}/u_{dc,\max} = 2k_2/5.19. \tag{45}$$

In general, the voltage ripple of virtual dc-link can be ignored when δ<5%, so k_2 should be less than 13%.

B. Power Factor and Cut-off Frequency Requirements

The input displacement angle of the novel qZS IMC is obtained as [20]

$$\begin{aligned}\theta_{\text{ind}} &= \arctan\frac{2\pi f_0 C u'}{I_{\text{rated}}} - \arctan\frac{2\pi f_0 L I_{\text{rated}}}{u'[1-4\pi^2 f_0^2 LC]} \\ &= \arctan\frac{2\pi f_0 C u_i}{(1-2D)I_{\text{rated}}} - \arctan\frac{2\pi f_0 (1-2D) L I_{\text{rated}}}{u_i\,[1-4\pi^2 f_0^2 LC]}.\end{aligned} \tag{46}$$

Therefore, the power factor is constrained as

$$\cos\theta_{\text{ind}} \geq pf_{\min} \tag{47}$$

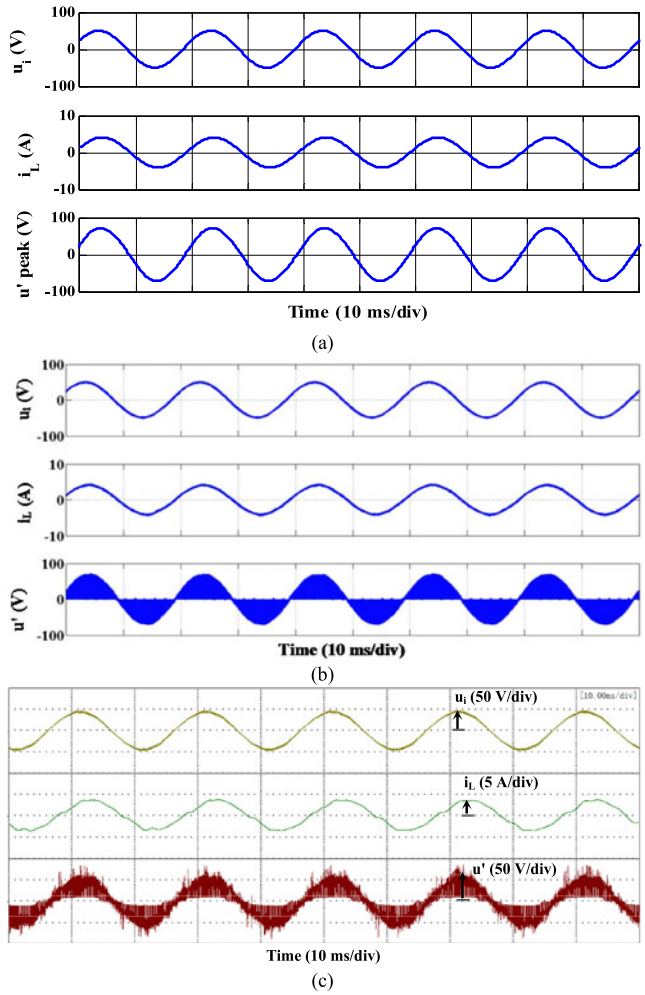

Fig. 11. Input voltage u_i, input current i_L, and output voltage u' of qZS-network when testing the novel qZS IMC. (a) Small-signal model-based results, (b) circuit simulation-based results, and (c) experimental results.

where $pf_{\min}$ denotes the minimum power factor.

From the small-signal analysis of filtering function in Section V and (39), the cut-off frequency ω_n of $G_{Lii}(s)$ should be less than one decade of the switching frequency, which provide the following constraint

$$\omega_n = \frac{1-2D}{\sqrt{LC}} \leq \frac{2\pi f_s}{10}. \tag{48}$$

From (42)–(48), following steps are used to design the qZS inductance and capacitance of the novel qZS IMC: 1) At the required grid voltage u_i ($i = a$, b, and c), the rated grid current I_{rated}, and shoot-through duty ratio D, the k_1 and k_2 are selected by $k_1 \leq 5\%$ and $k_2 \leq 13\%$ (referring to the aforementioned explanation) to compute L and C from (42) and (43) to limit the switching frequency voltage and current ripple within the required range; 2) then the calculated L and C from the step 1 are used to evaluate input power factor $\cos\theta_{\text{ind}}$ and the cut-off frequency ω_n according to (46)–(48); 3) if the $\cos\theta_{\text{ind}}$ is over the minimum power factor $pf_{\min}$ and the ω_n is less than one-tenth switching frequency, then the calculated L and C are confirmed; otherwise, L and C will be recalculated starting from the step 1 while regulating ripple limits k_1 and k_2.

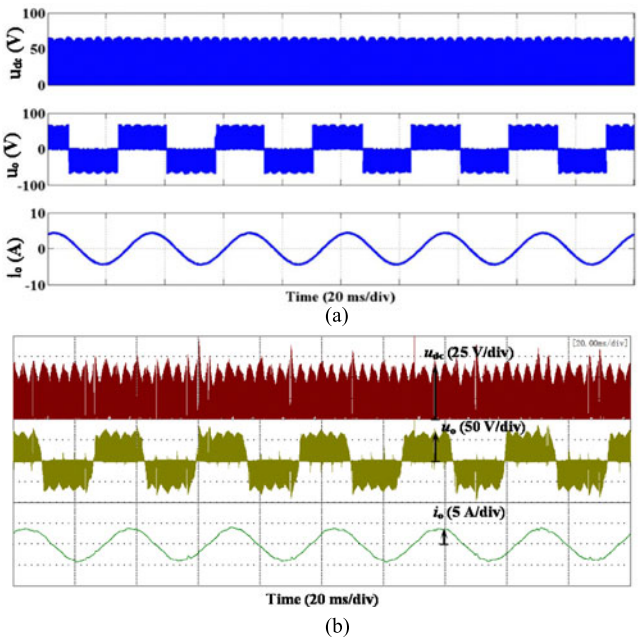

Fig. 12. DC-link voltage u_{dc}, output pulse voltage u_o, and load current i_o of the novel qZS IMC. (a) Simulation results and (b) experimental results.

VII. Simulation and Experimental Results

Simulation and experimental tests were performed to verify the analysis of the *LC*-filter-integrated qZS IMC shown in Fig. 4 and to compare the novel converter with the conventional qZS IMC and ZS IMC shown in Fig. 3(b) and (c). A 1.5-kW ZS/qZS IMC system is considered. Table I lists the parameters.

The grid voltage amplitude is 50 V; boosting factor $B = 2$, i.e., $D = 0.25$ and the output voltage amplitude of qZS network is 100 V; switching frequency $f_s = 10\,\text{kHz}$. For the qZS network parameters, $k_1 = 5\%$ and $k_2 = 10\%$ are iteratively confirmed by using the design method in Section VI, at which the qZS inductance $L = 1.9$ *m*H, qZS capacitance C=283 μF, power factor $\cos\theta_{\text{ind}} = 0.957$, and cut-off frequency $\omega_n = 687\,\text{rad/s}$. Therefore, the 2-*m*H qZS inductance and 300-μF qZS capacitance are selected in the prototype.

Fig. 10 shows the experimental setup. The controller is with digital signal processor executing the main algorithm and the complex programmable logic device extending the gate signals for the switches. A transformer is connected at the grid side to lower the grid voltage level before connecting to the ZS/qZS IMC. The experimental bench can be used to test the conventional qZS IMC and ZS IMC in Fig. 3(b) and (c), respectively, also to test the *LC*-filter-integrated qZS IMC in Fig. 4, through changing the connections and components.

A. Investigation of Modeling

The small-signal model in (11)–(21) is compared to circuit simulation and experimental results. Fig. 11(a), (b), and (c) shows the small-signal model-based results, circuit simulation-based results, and experimental results of qZS-network input voltage u_i, input current i_L, and output voltage u', respectively. Note that the qZS-network output voltage u', in Fig. 11(a) is the peak value envelope from the small-signal model. The same

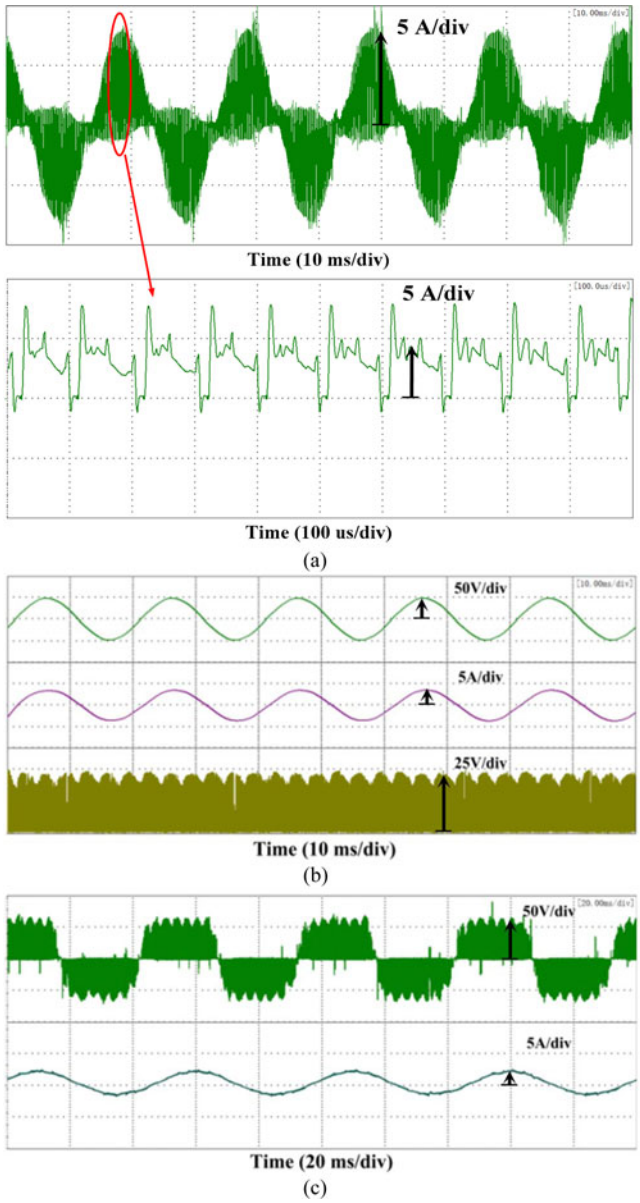

Fig. 13. Experimental results when testing the ZS IMC in Fig. 3(c). (a) Input current of ZS network, (b) grid voltage and current, dc-link voltage u_{dc}, and (c) output pulse voltage and load current.

50-V grid voltage amplitude and shoot-through duty cycle of 0.15 are performed to the three cases.

From Fig. 11, it can be seen that the small-signal model-based results, circuit simulation-based results, and experimental results well match each other, except that the qZS-network output voltage u' in experiment is little bit lower than the simulated voltage, which is caused by practical voltage drops on the inductors and power devices.

B. Voltage Gain Verification

Fig. 12(a) and (b) shows the circuit simulation-based results and experimental results of the *LC*-filter-integrated qZS IMC, where the 50-V grid voltage amplitude, 30-Hz output frequency, simple boost control, and shoot-through duty cycle of 0.15 are performed. When ignoring the stray resistance of inductors,

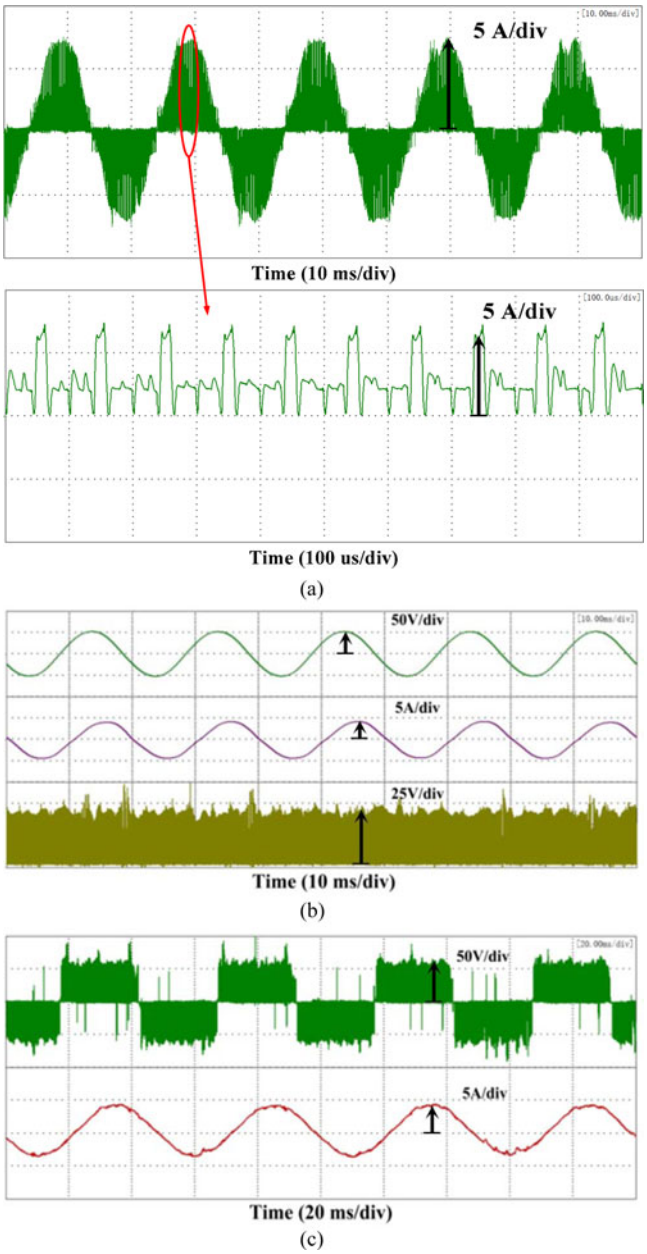

Fig. 14. Experimental results when testing the qZS IMC in Fig. 3(b). (a) Input current of qZS network, (b) grid voltage and current, dc-link voltage u_{dc}, and (c) output pulse voltage and load current.

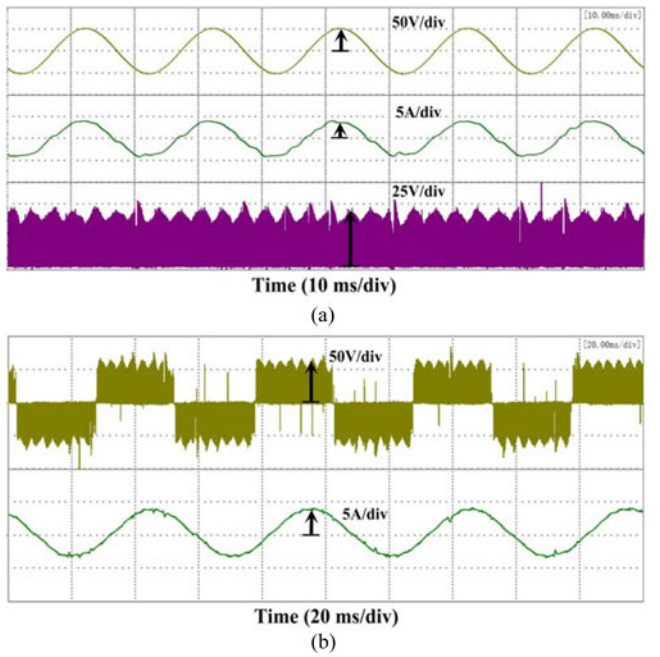

Fig. 15. Experimental results when testing the *LC*-filter-integrated qZS IMC in Fig. 4. (a) Grid voltage and current, dc-link voltage u_{dc}. Note: grid current is the input current of *LC*-filter-integrated qZS network and (b) output pulse voltage and load current.

from (31), the boost factor is 1.43. Simulated dc-link peak voltage is 71 V in Fig. 12(a), and the boost factor is $B = 71/50 = 1.42$. Experimental dc-link peak voltage is 69 V in Fig. 12(b), and the boost factor is 1.38. They are well identical to the theoretical values.

C. Filtering Function Verification

In order to investigate the filtering ability of ZS/qZS/*LC*-filter-integrated-qZS network, in the ZS-IMC/qZS-IMC/*LC*-filter-integrated-qZS-IMC shown in Figs. 3(c), (b), and 4, the input currents of ZS network, qZS network, and *LC*-filter-integrated qZS network are specially shown in Figs. 13–15, respectively, during performing experiments of three converter systems.

The input current of ZS network when testing ZS IMC in Fig. 3(c) shows discontinuous waveform and high harmonics with THD of 55.61%, as shown in Fig. 13(a); for the qZS IMC in Fig. 3(b), the discontinuous input current of qZS network also causes high harmonics with THD of 58.06%, as shown in Fig. 14(a). However, in the test of *LC*-filter-integrated qZS IMC in Fig. 4, the continuous input current of *LC*-filter-integrated qZS network results in a low harmonic waveform with THD of 5.22%, as shown in Fig. 15(a).

From Figs. 13–15, it can be seen that the *LC*-filter-integrated qZS IMC can be directly connected to the grid without additional input filter, as shown in Fig. 4, because of filtering function of the *LC*-filter-integrated qZS network. However, for the other two topologies, i.e., the qZS IMC and ZS IMC shown in Fig. 3(b) and (c), the ZS network and qZS network cannot be directly connected to the grid, and additional input filters are necessary between the grid and ZS/qZS network, as shown in Fig. 3. In fact, the additional input filter consisted of 3-mH filter inductance and 50-μF filter capacitance is employed to smooth the grid current satisfying the THD standard (less than 5%) in testing the qZS IMC and ZS IMC shown in Fig. 3(b) and (c). Additional input filter and ZS/qZS network cause the qZS IMC and ZS IMC shown in Fig. 3(b) and (c) to have high cost, high volume, high loss, and high weight, when compared to the novel qZS IMC in Fig. 4.

Figs. 13(b) and 14(b) show the grid currents, which show the low harmonic waveforms with THDs of 2.08% and 2.94%, respectively. However, the efficiencies of the *LC*-filter-integrated qZS IMC, ZS IMC, and qZS IMC are 89.67%, 88.83%, and 83.61%, respectively, which shows that additional input filters cause more loss from the ZS IMC and qZS IMC.

Figs. 13(c), 14(c), and 15(b) show the 20-Hz load currents and pulse voltages from the ZS IMC, qZS IMC, and novel qZS IMC,

respectively. Fig. 13(c) shows a lower load current compared to Figs. 14(c) and 15(b), because the ZS IMC in Fig. 3(c) has lower voltage gain than the qZS IMC in Fig. 3(b) and the novel qZS IMC in Fig. 4.

VIII. Conclusion

An in-depth investigation was conducted on small-signal modeling, voltage gain, filtering function, and parameters design of the *LC*-filter-integrated qZS IMC in this paper. The novel qZS IMC linked the qZS network between the grid and the IMC bridge. Second-order input filtering was achieved without the need for a dedicated input filter and voltage boost capability was achieved that extended the voltage gain of IMC beyond the traditional limit of 0.866. The small-signal modeling of qZS network was presented. Based on that, the voltage gain was derived, the filtering capability was analyzed, and the qZS inductance and capacitance were designed for the novel qZS IMC. A prototype was built to validate the theoretical analysis and parameters design method. The small-signal model was verified by comparing with circuit simulation-based results and experimental results. The voltage gains in simulation and experiment matched the calculated results. At the designed impedance parameters, the input current waveforms and THD of the *LC*-filter-integrated qZS IMC were compared with those of conventional ZS IMC and qZS IMC. The results demonstrated continuous input current and much low THD of the novel qZS IMC, verifying its filtering function.

References

[1] S. Safari, A. Castellazz, and P. W. Wheeler, "Experimental and analytical performance evaluation of SiC power devices in the matrix converter," *IEEE Trans. Power Electron.*, vol. 29, no. 5, pp. 2584–2596, May 2014.

[2] C. Xia, J. Zhao, Y. Yan, and T. Shi, "A novel direct torque control of matrix converter fed PMSM drives using duty cycly control for torque ripple reduction," *IEEE Trans. Ind. Electron.*, vol. 61, no. 6, pp. 2700–2713, Jun. 2014.

[3] T. D. Nguyen and L. Hong-Hee, "Dual three-phase indirect matrix converter with carrier-based PWM method," *IEEE Trans. Power Electron.*, vol. 29, no. 2, pp. 569–581, Feb. 2014.

[4] L. Empringham, J. W. Kolar, J. Rodriguez, P. W. Wheeler, and J. C. Clare, "Technological issues and industrial application of matrix converters: A review,"*IEEE Trans. Ind. Electron.*, vol. 60, no. 10, pp. 4260–4271, Oct. 2013.

[5] Y. D. Yoon and S. K. Sul, "Carrier-based modulation technique for matrix converter," *IEEE Trans. Power Electron.*, vol. 21, no. 6, pp. 1691–1703, Nov. 2006.

[6] G. T. Chiang and J. Itoh, "Comparison of two over modulation strategies in an indirect matrix converter," *IEEE Trans. Ind. Electron.*, vol. 60, no. 1, pp.43–53, Jan. 2013.

[7] O. Ellabban, H. Abu-Rub, and S. Bayhan, "Z-source matrix converter: An overview," *IEEE Trans. Power Electron.*, to be published, doi: 10.1109/TPEL.2015.2471799.

[8] P. Szczesniak, *Three-Phase AC-AC Power Converters Based on Matrix Converter Topology, Matrix-Reactance Frequency Converters Concept*. London, U.K.: Springer-Verlag, 2013.

[9] F. Z. Peng, "Z-source inverter," *IEEE Trans. Ind. Appl.*, vol. 39, no. 2, pp. 504–510, Mar./Apr. 2003.

[10] J. Anderson and F. Z. Peng, "Four quasi-Z-Source inverters," in *Proc. 39th IEEE Annu. Power Electron. Spec. Conf.*, Rhodes, Greece, 2008, pp. 2743–2749.

[11] Y.P. Siwakoti, F.Z. Peng, F. Blaabjerg, P. C. Loh, and G.E. Town, "Impedance-source networks for electric power conversion Part I: A topological review," *IEEE Trans. Power Electron.*, vol. 30, no. 2, pp. 699–716, Feb. 2015.

[12] W. Song, Y. Zhong, H. Zhang, X. Sun, Q. Zhang, and W. Wang, "A study of Z-source dual-bridge matrix converter immune to abnormal input voltage disturbance and with high voltage transfer ratio," *IEEE Trans. Ind. Informat.*, vol. 9, no. 2, pp. 828–838, May 2013.

[13] X. Liu, P. C. Loh, P. Wang, and X. Han, "Improved modulation schemes for indirect Z-source matrix converter with sinusoidal input and output waveforms," *IEEE Trans. Power Electron.*, vol. 27, no. 9, pp. 4039–4050, Sep. 2012.

[14] E. Karaman, M. Farasat, and A.M. Trzynadlowski, "Permanent-magnet synchronous-generator wind-energy systems with boost matrix converters," in *Proc. IEEE Energy Convers. Congr. Expo.*, Sep. 15–19, 2013, pp. 2977–2981.

[15] T.D. Nguyen, H.M. Nguyen, H. Lee, and T. Chun, "An approach of sparse matrix converter using Z-source network," in *Proc. Int. Power Electron. Conf.*, Jun. 21–24, 2010, pp. 2774–2780.

[16] K. Park, K. Lee, and F. Blaabjerg, "Improving output performance of a Z-source sparse matrix converter under unbalanced input-voltage conditions," *IEEE Trans. Power Electron.*, vol. 27, no. 4, pp. 2043–2054, Apr. 2012.

[17] B. Ge, Q. Lei, W. Qian, and F. Z. Peng, "A family of Z-source matrix converters," *IEEE Trans. Ind. Electron.*, vol. 59, no. 1, pp. 35–45, Jan. 2012.

[18] S. Liu, B.Ge, H. Abu-Rub, and F. Z. Peng, "Modeling, analysis, and motor drive application of quasi-Z-source indirect matrix converter," *COMPEL: Int. J. Comput. Math. Elect. Electron. Eng.*, vol. 33, no. 1/2, pp. 28–28, 2013.

[19] S. Liu, B. Ge, X. Jiang, H. Abu-Rub, and F. Z. Peng, "Comparative evaluation of three Z-source/quasi-Z-source indirect matrix converters," *IEEE Trans. Ind. Electron.*, vol. 62, no. 2, pp. 692–701, Feb. 2015.

[20] A.K. Sahoo, K. Basu, and N. Mohan, "Systematic input filter design of matrix converter by analytical estimation of RMS current ripple," *IEEE Trans. Ind. Electron.*, vol. 62, no. 1, pp.132–143, Jan. 2015.

[21] *IEEE Recommended Practices and Requirements for Harmonic Control in Electrical Power Systems*, IEEE 519, 1992.

Shuo Liu received the M.S. and Ph.D. degrees in electrical engineering from the North China University of Technology and Beijing Jiaotong University, Beijing, China, in 2011 and 2015, respectively.

He is currently an Assistant Professor in the Department of Electrical Engineering, North China University of Technology. His research interests include Z-source converter, matrix converter, and motor drives.

Baoming Ge (M'11) received the Ph.D. degree in electrical engineering from Zhejiang University, Hangzhou, China, in 2000.

He was with the Department of Electrical Engineering, Tsinghua University, Beijing, China, from 2000 to 2002. In 2002, he joined the School of Electrical Engineering, Beijing Jiaotong University, Beijing, where he was promoted to Professor in 2006. He was with the University of Coimbra, Coimbra, Portugal, from 2004 to 2005, and with Michigan State University, East Lansing, MI, USA, from 2007 to 2008 and 2010 to 2014. He is with the Renewable Energy and Advanced Power Electronics Research Laboratory, Department of Electrical and Computer Engineering, Texas A&M University, College Station, TX, USA. He has authored more than 200 journal and conference papers, two books, two book chapters, holds seven patents. His main research interests include the renewable energy generation, electrical machine drives, and power electronics.

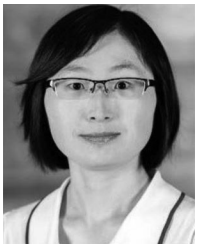

Yushan Liu (S'12–M'15) received the B.Sc. degree in automation from the Beijing Institute of Technology, Beijing, China, in 2008, and the Ph.D. degree in electrical engineering from the School of Electrical Engineering, Beijing Jiaotong University, Beijing, in 2014.

She is currently a Postdoctoral Research Associate in the Department of Electrical and Computer Engineering, Texas A&M University at Qatar, Doha, Qatar, where she was a Research Assistant from 2011 to 2014. She has published more than 45 journal and conference papers, one book, and one book chapter in the area of expertise. Her research interests include impedance-source inverters, cascade multilevel converters, photovoltaic power integration, renewable energy systems, pulsewidth modulation techniques, etc.

Dr. Liu is the recipient of "*Research Fellow Excellence Award*" from Texas A&M University at Qatar, one of "*Excellent Ten Doctoral Dissertations*" from Beijing Jiaotong University, and many other prestigious research awards.

Haitham Abu-Rub (M'99–SM'07) received two Ph.D. degrees, one in electrical engineering and another in humanities, in 1995 and 2004, respectively.

Since 2006, he has been associated with Texas A&M University at Qatar, Doha, Qatar, where he was promoted to Professor. He is currently the Chair of Electrical and Computer Engineering Program at the same university as well as the Managing Director of Smart Grid Center–Extension in Qatar. He has published more than 250 journal and conference papers, and has earned and supervised many research projects. He is currently leading many potential projects on photovoltaic and hybrid renewable power generation systems with different types of converters and on electric drives. He is co-author of four books, three of which are with Wiley. He is also an author/co-author of five book chapters. His main research interests are energy conversion systems, including electric drives, power electronic converters, renewable energy and smart grid.

Robert S. Balog (S'92–M'96–SM'07) received the B.S. degree from Rutgers, The State University of New Jersey, New Brunswick, NJ, USA, in 1996, and the M.S. and Ph.D. degrees from the University of Illinois at Urbana-Champaign, Urbana, IL, USA, in 2002 and 2006, respectively, all electrical engineering.

From 1996 to 1999, he was an Engineer with Lutron Electronics, Coopersburg, PA, USA. From 2005 to 2006, he was a Researcher with the U.S. Army Corp of Engineers, Engineering Research and Development Center, Construction Engineering Research Laboratory, Champaign, IL, USA. From 2006 to 2009, he was a Senior Engineer at SolarBridge Technologies, Champaign, IL, USA (acquired by Sunpower Corp in 2014). He then joined Texas A&M University, College Station, TX, USA, where he is currently an Associate Professor with tenure in the Department of Electrical and Computer Engineering and Director of the Renewable Energy and Advanced Power Electronics Research Laboratory. He holds a joint faculty appointment with Texas A&M University at Qatar where he is currently in-residence. He holds 17 issued and pending U.S. patents. He is co-author of the book *Microgrids and Other Local Area Power and Energy Systems* (Cambridge, U.K.: Cambridge Univ. Press, 2016). His current research interests include power converters and balance-of-systems technologies for solar photovoltaic energy, particularly microinverters for ac photovoltaic modules, and highly reliable electrical power and energy systems including dc microgrids.

Dr. Balog is a Registered Professional Engineer in the State of Illinois. He is currently serving as an elected Member-at-Large for the Power Electronics Society Administrative Committee and has previously served as the Chair of the Membership committee and Graduates of the Last Decade committee. He is the Technical Program Chair for the 2016 IEEE Energy Conversion Congress and Exposition. He received the inaugural IEEE Joseph J. Suozzi INTELEC Fellowship in 2001. He has been a member of Eta Kappa Nu, Sigma Xi, National Society of Professional Engineers, American Solar Energy Society, and Solar Electric Power Association. He was recognized as an external member of the Hungarian Academy of Science in 2011 and was the recipient of the 2011 Rutgers College of Engineering Distinguished Engineer Award.

Hexu Sun (M'90–SM'96) received the Ph.D. degree in automation from Northeastern University, Shenyang, China, in 1993.

He has been a Professor with the School of Control Science and Engineering, Hebei University of Technology, Tianjin, China, and also with the School of Electrical Engineering, Hebei University of Science and Technology, Shijiazhuang, China. He has authored five books, more than 130 journal and conference papers, and holds 13 patents and five Computer Software Copyrights. His research interests include motion control theory and technology, complex engineering system and its control technology, networked control system, embedded control system, wind power, and renewable energy system.

Dr. Sun is the invited Plenary Speaker and General Co-Chair of many international conferences. He was the Director in many societies and committees in China. He was the recipient of many prestigious national awards from China.